Proceedings of the 21st ICSMGE, Vienna, Austria, 14 – 19 June 2026. Pistrol, Adam & Schweiger (eds.)
Published by: ÖGG, Austrian Society for Geomechanics, Salzburg, Austria, ISBN 978-3-9503898-4-5
https://doi.org/10.53243/ICSMGE2026-157

Post-liquefaction shear deformation of granular material under different initial states and loading conditions

Qizhuo Yang, Jian-Min Zhang, and Rui Wang
Department of Hydraulic Engineering, State Key Laboratory of Hydroscience and Engineering, Tsinghua University, Beijing, China

ABSTRACT: Large post-liquefaction shear deformation is a critical phenomenon in soil liquefaction. The study investigates the influence of initial states and loading conditions on post-liquefaction deformation, aiming to identify micro scale features governing liquefaction behavior. Three-dimensional discrete element method (DEM) is adopted to conduct numerical undrained cyclic triaxial tests on specimens with varying initial fabrics under different intermediate principal strain coefficients (b_ε). The DEM simulations can capture the typical macro and micro scale liquefaction behavior of granular materials under cyclic and constant b_ε loading conditions. The role of features such as void ratio, particle orientation fabric anisotropy, contact normal fabric anisotropy, coordination number, and redundancy index are found to be not the determining factors for liquefaction induced shear strain. Instead, the mean neighboring particle distance (*MNPD*), a fabric measure originally proposed by Wang et al. (2016) in two-dimensional analyses, emerges as the primary factor governing post-liquefaction shear strain under both cyclic and constant b_ε loading conditions. Furthermore, the initial *MNPD* is found to be a reliable indicator the final saturated post-liquefaction shear deformation that can be generated under undrained cyclic loading, for all initial states and loading conditions considered in this study.

KEYWORDS: DEM, shear deformation, fabric, intermediate principal strain.

1 INTRODUCTION

Liquefaction is a phenomenon wherein saturated sand loses its shear strength, and changes behavior from solid-like to liquid-like. The significant deformation induced by liquefaction can cause severe damage. Therefore, to gain a deep understanding of liquefaction deformation, it is essential to investigate its dependency on initial conditions and loading conditions.

Large shear strain following initial liquefaction has consistently been oberserved in laboratory element tests (De Alba et al., 1976; Zhang et al., 1997; Zhang & Wang, 2024). It is found that shear strain generated at near zero effective stress (termed γ_0) accumulates with increasing loading cycles, ultimately reaching a saturated state, and the macro physical interpretation of the large post-liquefaction deformation is provided by Zhang and Wang (2012).

With the development of the discrete element method (DEM), increasing research has explored the micro mechanisms of post-liquefaction deformation at the particle scale. Wang and Wei (2016) proposed the concept of "centroid distance" fabric through two-dimensional (2D) DEM simulations, revealing a strong correlation between this particle-void fabric and post-liquefaction deformation. Wang et al., (2016) introduced a new fabric measure, the Mean Neighbouring Particle Distance (*MNPD*), using 2D DEM simulations. It is found that the peak *MNPD* in each loading cycle uniquely correlates to the shear strain induced by liquefaction within each cycle. Subsequently, Yang et al. (2025) conducted undrained cyclic triaxial simulations, demonstrating that *MNPD* effectively governs the evolution of post-liquefaction shear strain in 3D, and established a unique relationship between initial *MNPD* and saturated post-liquefaction shear deformation. However, conventional cyclic triaxial or biaxial tests impose axisymmetric stress conditions, which differ markedly from complex natural loading scenarios, such as those induced by traffic loads, waves, or earthquakes. Thus, examining post-liquefaction deformation under non-axisymmetric stress conditions with varying intermediate principal strain coefficients (b_ε) holds significant theoretical and practical value.

This study employs 3D discrete element method to conduct cyclic true triaxial simulations, investigating the effects of initial conditions and loading modes on post-liquefaction deformation in specimens with diverse initial states under constant b_ε and cyclic b_ε loading modes.

2 MODEL SETUP

2.1 *Specimen preparation and simulation procedures*

This study employs the open-source LIGGGHTS software for three-dimensional discrete element simulations (Kloss et al., 2012). Clump particles with an aspect ratio of 1.5:1 are used, with particle sizes uniformly distributed between 1 and 3 mm. The Hertz-Mindlin model is adopted to describe the particle contact behaviour. The Young's modulus is 20 GPa, the Possion's ratio is 0.22, the coefficient of restitution is 0.87, and the inter-particle coefficient is 0.5.

Four types of specimens with distinct initial fabric structures are obtained through different specimen preparation methods, designated as ANIs, ANIm, ANIw, and ISO, representing strong anisotropic, medium anisotropic, weak anisotropic, and isotropic, respectively. Each numerical specimen contains approximately 5,000 clumped particles. The detailed specimen preparation procedure is described in Yang et al. (2025) and is not repeated here.

The specimens undergo isotropic consolidation at 100 kPa, with the friction coefficient between particles adjusted during the consolidation process to achieve varied initial states, which is restored to the prescribed value before loading. The initial void ratio, coordination number, and particle orientation anisotropy for the 14 specimens are detailed in Table 1. To consistently characterize the loading path in cyclic true triaxial tests, this study employs the intermediate principal strain coefficient (b_ε), defined as $b_\varepsilon = (\varepsilon_2 - \varepsilon_3) / (\varepsilon_1 - \varepsilon_3)$.

Table 1. Specimen ID and initial parameters

Specimen ID	Void ratio e	Initial particle orientation fabric anisotropy intensity a_{pin}	Initial coordination number C_{in}
ISO_e56_C474	0.562	0.015	4.742
ISO_e58_C434	0.582	0.013	4.342
ISO_e59_C398	0.594	0.015	3.981
ANIw_e56_C494	0.560	0.087	4.936
ANIw_e58_C489	0.581	0.069	4.892

ANIw_e60_C443	0.603	0.078	4.431
ANIw_e62_C406	0.619	0.081	4.065
ANIw_e63_C383	0.625	0.097	3.827
ANIm_e43_C471	0.435	0.097	4.707
ANIm_e44_C469	0.442	0.098	4.865
ANIm_e45_C423	0.453	0.098	4.234
ANIm_e46_C396	0.464	0.093	3.962
ANIm_e48_C379	0.484	0.102	3.786
ANIs_e47_C395	0.469	0.201	3.952

2.2 *Different loading conditions:cyclic b_ε and constant b_ε*

After consolidation, the 14 groups of specimens are subjected to two types of undrained cyclic true triaxial loading: constant b_ε and cyclic b_ε. Figure 1 presents schematic diagrams illustrating these loading modes, with arrow lengths indicating the relative magnitudes of wall movement rates in each direction.

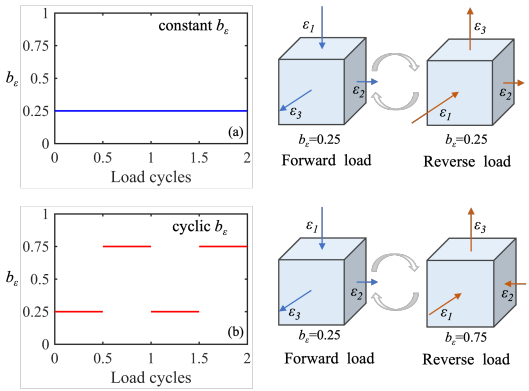

Figure 1. Schematic diagram of two different loading modes with b_ε = 0.25 as an example (a) constant b_ε loading; (b) cyclic b_ε loading

Taking b_ε = 0.25 as an example (Figure 2a), in the constant b_ε value loading mode, when the specimen reaches an deviatoric stress amplitude of 30 kPa, all six walls maintain their original loading rates but reverse loading direction until the specimen returns to a hydrostatic state. Subsequently, the top and bottom walls reverse their loading direction, while the four horizontal walls adjust both direction and rate to maintain a constant b_ε value, repeating the cycle. In the cyclic b_ε loading mode, when the specimen reaches a shear stress amplitude of 30 kPa, all six walls maintain their original loading rates but reverse direction until the deviatoric stress amplitude again reaches 30 kPa, continuing cyclically. Conventional undrained cyclic triaxial tests correspond to the cyclic b_ε loading mode with b_ε = 0. The initial vertical loading rate is set at a strain rate of 0.0008 s^{-1}, with horizontal loading rates calculated based on the constant volume condition and the b_ε value to determine lateral wall movement rates. The specimen's inertia number during simulation is 4.2×10^{-5}, which is less than 0.001, satisfying quasi-static conditions (Da Cruz et al., 2005). Liquefaction is deemed to occur when the mean effective stress p falls below $0.01p_0$ (Wang et al., 2016). To investigate the deformation mechanisms post-liquefaction, all simulations in this study are stopped after 15 loading cycles after the onset of liquefaction.

2.3 *Calculation of stress, strain, and fabric quantities.*

In this study, the mean effective stress is defined as $p = (\sigma_1 + \sigma_2 + \sigma_3)/3$. The deviatoric stress q and equivalent shear strain γ can be obtained by Eq. (1) and (2), respectively. These definitions conventionally yield positive values. To differentiate loading and reverse loading in cyclic true triaxial tests, signs are assigned following geomechanics conventions, with compressive stress and strain denoted as positive.

$$q = \mathrm{sign}(\varepsilon_z)\sqrt{\frac{1}{2}\left\{(\sigma_x-\sigma_y)^2+(\sigma_y-\sigma_z)^2+(\sigma_z-\sigma_x)^2\right\}} \quad (1)$$

$$\gamma = \mathrm{sign}(\varepsilon_z)\frac{\sqrt{2}}{3}\sqrt{(\varepsilon_x-\varepsilon_y)^2+(\varepsilon_y-\varepsilon_z)^2+(\varepsilon_z-\varepsilon_x)^2} \quad (2)$$

The coordination number is a critical fabric which is widely used to characterize the load-bearing structure of granular materials. It is defined as $C = 2N_c/N_p$, where N_c is the number of contacts and N_p is the number of particles.

The redundancy index (*RI*) quantifies the mechanical constraint of interparticle contacts on particle kinematics, defined as the ratio of total constraints to available degrees of freedom. Following Huang et al. (2018), *RI* is expressed as $RI = (3\text{-}2f)N_c/[6(N_p\text{-}N_p^0)]$, where N_p^0 is the number of non-contacting "rattlers", and f is the sliding fraction. This metric excludes floating particles to focus on force-transmitting networks.

The particle-orientation fabric tensor $\mathbf{F_p}$ and the contact-normal fabric tensor $\mathbf{F_c}$ are defined based on Satake (1982):

$$\boldsymbol{F_p} = \frac{1}{N_p}\sum_{k=1}^{N_p}\boldsymbol{v_p^k}\otimes\boldsymbol{v_p^k}, \quad \boldsymbol{F_c} = \frac{1}{N_c}\sum_{k=1}^{N_c}\boldsymbol{v_c^k}\otimes\boldsymbol{v_c^k} \quad (3)$$

where $\boldsymbol{v_p^k}$ is the unit particle orientation vector of the kth clump; $\boldsymbol{v_c^k}$ is the unit normal vector of the kth contact, and $\otimes$ denotes the tensor product.

To quantify the degree of anisotropy, the particle-orientation fabric anisotropy intensity a_p and the contact-normal fabric anisotropy intensity a_c are calculated as follows:

$$a_p = \sqrt{\frac{1}{2}\left[(F_{p1}-F_{p2})^2+(F_{p2}-F_{p3})^2+(F_{p3}-F_{p1})^2\right]} \quad (4)$$

$$a_c = \sqrt{\frac{1}{2}[(F_{c1}-F_{c2})^2+(F_{c2}-F_{c3})^2+(F_{c3}-F_{c1})^2]} \quad (5)$$

where F_{p1}, F_{p2}, F_{p3} are the eigenvalues of $\mathbf{F_p}$, and F_{c1}, F_{c2}, F_{c3} are the eigenvalues of $\mathbf{F_c}$. Values of a_p or a_c equal to zero indicate isotropy, while increasing values reflect greater anisotropy.

The "Mean Neighboring Particle Distance" (*MNPD*) is a fabric scalar characterizing microstructural attributes influencing post-liquefaction deformation in 2D DEM simulations (Hu et al., 2020; Wang et al., 2016). It is calculated as the normalized mean Neighboring Particle Distance (*NPD*) of particles in a specimen. For each particle, *NPD* is the average surface-to-surface distance to its n nearest neighbor particles. n is the number of contacts required to form a stable load-bearing structure. For 3D case, n=4 has been verified, and the *MNPD* is described by Yang et al. (2025):

$$MNPD = \frac{1}{N_p * d_{50}}\sum_{k=1}^{N_p}\frac{D1^k+D2^k+D3^k+D4^k}{4} \quad (6)$$

where d_{50} is the average particle diameter, and $D1^k$, $D2^k$, $D3^k$, $D4^k$ are the surface-to-surface distances to the four nearest neighbors of the kth particle, respectively.

3 TYPICAL DEM RESULTS

Figure 2 depicts the stress path and stress-strain relationship for specimen ANIw_e62_C406 under constant and cyclic b_ε loading modes at b_ε = 0, 0.5, and 1. The macroscopic responses

across different b_ε values are generally consistent. Before liquefaction, the mean effective stress p decreases with increasing loading cycles until liquefaction occurs. In the post-liquefaction stage, the stress path displays a repetitive "butterfly" pattern, with shear strain at zero effective stress (γ_0) rapidly increasing and stabilizing at a bounded value. It is suggested that, for the same specimen with identical initial state, increasing b_ε slightly reduces liquefaction resistance under constant b_ε loading, whereas variations in b_ε values have minimal impact on liquefaction resistance under cyclic b_ε loading.

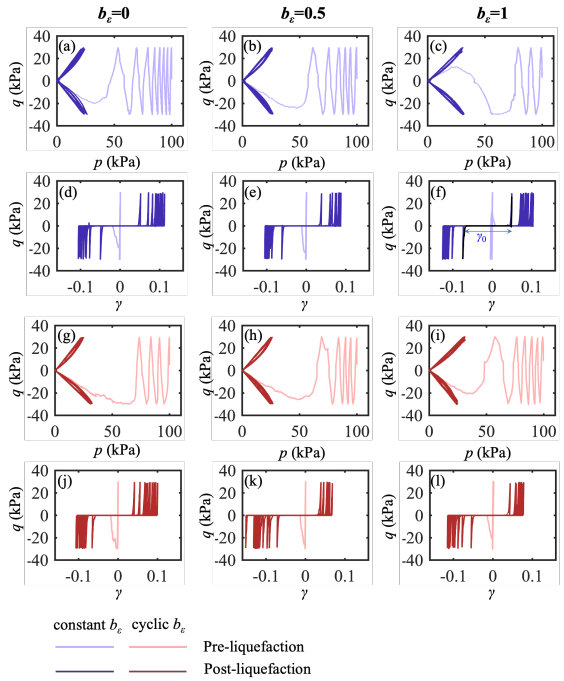

Figure 2. Stress path and stress-strain curve of specimen ANIw_e62_C406 under constant and cyclic b_ε loading mode when b_ε=0,0.5, and 1.

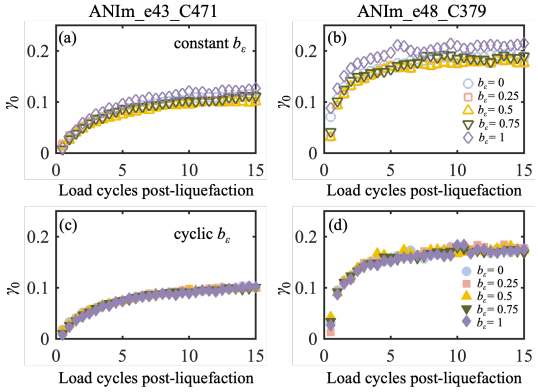

Figure 3. Evolution of post-liquefaction shear strain γ_0 with load cycles post-liquefaction for specimens ANIm_e43_C471 and ANIm_e48_C379 under two loading conditions: (a),(b) constant b_ε loading; (c),(d) cyclic b_ε loading.

Figure 3 illustrates the evolution of post-liquefaction shear strain with loading cycles for specimens ANIm_e43_C471 and ANIm_e48_C379 with varying initial fabric structures under constant and cyclic b_ε loading modes at b_ε = 0, 0.25, 0.5, 0.75, and 1. The saturated post-liquefaction shear strain (γ_{0s}) of specimen ANIm_e43_C471 is significantly higher than that of specimen ANIm_e48_C379 under both loading conditions, reflecting the influence of initial fabric properties. Although the initial void ratio affects γ_{0s} under the same specimen preparation method, prior studies have indicated that it is not the sole determinant (Wang et al., 2016; Yang et al., 2025). Constant and cyclic b_ε loading modes exhibit a consistent trend that γ_0 initially increases and then stabilizes. Comparing Figure 3b and Figure 3d, γ_{0s} under cyclic b_ε loading are nearly identical across different b_ε values, whereas under constant b_ε loading, γ_0 shows slight variations, with b_ε = 1 and b_ε = 0 yielding marginally greater γ_{0s} than other b_ε, while b_ε = 0.5 produces the smallest γ_{0s}.

4 POST-LIQUEFACTION SHEAR DEFORMATION

In conventional cyclic triaxial simulations, it is proven that the coordination number, redundancy index, particle orientation fabric anisotropy intensity, and contact normal fabric anisotropy strength do not adequately reflect the evolution of post-liquefaction shear deformation γ_0. Instead, the maximum *MNPD* ($MNPD_{max}$) per cycle exhibits a strong correlation with shear strain (γ_0). Previous studies have revealed that as the mean effective stress p decreases to zero, *MNPD* initially increases with γ, reaching its peak value ($MNPD_{max}$) under zero effective stress state within each half-cycle, then *MNPD* decreases with γ, ultimately bringing the material out of liquefaction state. To evaluate this $MNPD_{max}$-γ_0 relationship under varying b_ε loading conditions, this study plots the $MNPD_{max}$ against γ_0 for each post-liquefaction loading cycle for specimens with various initial fabrics under constant and cyclic b_ε loading modes in Figure 4. The results demonstrate that $MNPD_{max}$ effectively reflects the γ_0 evolution under both loading modes. A second-order polynomial fitting to 2,100 data points yields a coefficient of determination (R^2) of 0.811 for constant b_ε loading and 0.857 for cyclic b_ε loading, indicating a strong correlation between $MNPD_{max}$ and γ_0. Under constant b_ε loading, the slightly weaker correlation is attributed to minor variations in γ_0 across different b_ε values, with γ_0 being greatest for b_ε = 1, followed by b_ε = 0, and lowest for b_ε = 0.5. These variations likely stem from differences in *MNPD* evolution across various b_ε values. Thus, it is suggested that while $MNPD_{max}$ primarily governs the γ_0 under constant b_ε loading, the specific loading path also exerts a subtle influence on the evolution of γ_0.

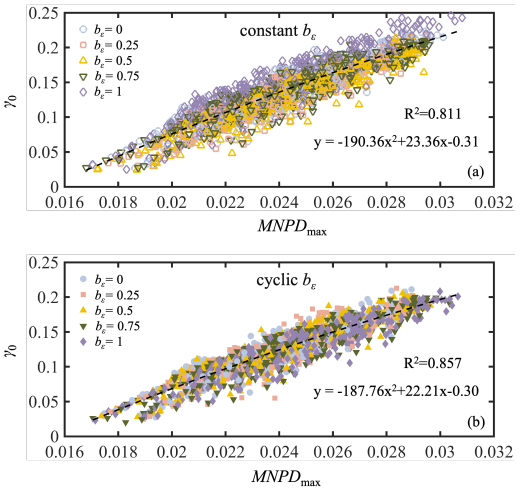

Figure 4. Correlation between γ_0 and $MNPD_{max}$ in each half-loading cycle post-liquefaction across 14 tests under two different loading modes.(a) constant b_ε loading; (b) cyclic b_ε loading.

Figure 5 illustrate the broader relationship between saturated post-liquefaction shear strain (γ_{0s}) and conventional initial fabric characteristics for 14 specimens under constant b_ε loading conditions, as cyclic b_ε loading results closely resemble those of conventional cyclic triaxial tests due to nearly identical γ_{0s} across different b_ε. Figure 5a and b show no significant

correlation between γ_{0s} and initial particle-orientation fabric anisotropy intensity a_{pin} or initial contact normal fabric anisotropy intensity a_{cin}. A negative trend is observed between γ_{0s} and initial coornidation number C_{in} or initial rendundancy index RI_{in} in Figure 5c and d, however, prior studies have indicated that this correlation is not unique, particularly for specimens experienced reconsolidation in post-liquefaction stage. Figure 5e indicates no unique relationship between initial void ratio e_{in} and γ_{0s}, as specimens with different void ratios, such as ANIw_e60_C433 and ANIs_e47_C395, exhibit similar γ_{0s} (0.1698 and 0.1692, respectively), under constant b_ε loading across various b_ε values.

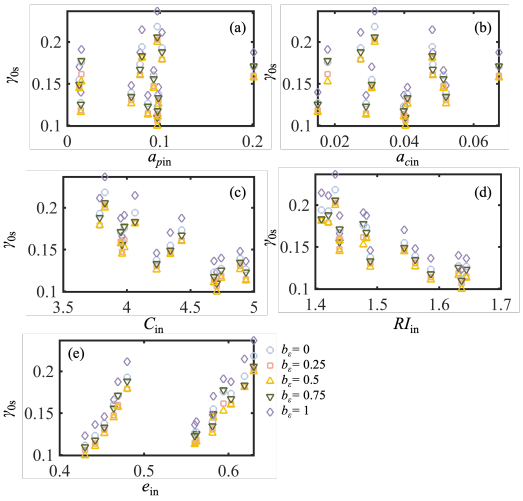

Figure 5. Correlation between initial conventional fabric quantities and saturated post-liquefaction shear strain γ_{0s} under constant b_ε loading condition: (a) initial particle orientation fabric anisotropy intensity a_{pin}; (b) initial contact normal fabric anisotropy intensity a_{cin}; (c) initial coordination number C_{in}; (d) initial redundancy index RI_{in} (e) initial void ratio.

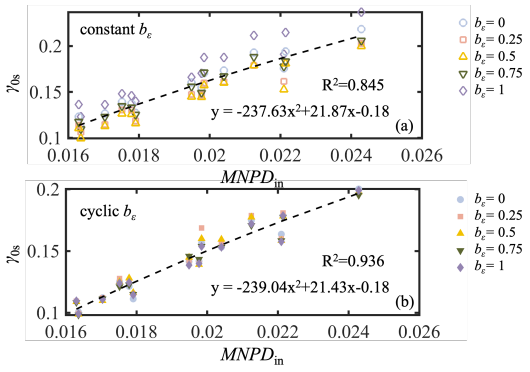

Figure 6. Correlation between γ_{0s} and $MNPD_{in}$ under two different loading modes.(a) constant b_ε loading; (b) cyclic b_ε loading.

In contrast, Figure 6 illustrates a strong correlation between the initial *MNPD* value and saturated shear strain post-liquefaction γ_{0s} under both constant b_ε and cyclic b_ε loading modes. A second order polynomial fit for 14 specimens under constant b_ε loading yields a coefficient of determination R^2 of 0.845, while cyclic b_ε loading achieves a slightly higer R^2 of 0.936. As depicted in Figure 6a, under constant b_ε = 1, the specimen undergoes triaxial extension, resulting in slightly larger γ_{0s} values and some data dispersion compared to other b_ε values. These findings indicate that the $MNPD_{in}$ effectively predicts γ_{0s} across diverse initial states and complex loading scenarios. The robust relationship supports the incorporation of $MNPD_{in}$ into continuum-based constitutive models with appropriate formulations, offering significant implications for earthquake geotechnical engineering.

5 CONCLUSIONS

This study employs the 3D discrete element method to conduct cyclic undrained triaxial tests on specimens with diverse initial fabric under constant and cyclic b_ε loading modes with varing intermediate principal strain coefficient (b_ε = 0, 0.25, 0.5, 0.75, and 1). The main conclusions are as follows:

(1) Under non-axisymmetric stress conditions, the evolution of the $MNPD_{max}$ governs the development of post-liquefaction shear strain γ_0 regardless of initial states. The specific value of the loading path slightly affects the $MNPD_{max}$-γ_0 relationship, especially under constant b_ε loading modes.

(2) A strong correlation between the initial *MNPD* ($MNPD_{in}$) and the saturated post-liquefaction shear strain γ_{0s} is identified under both constant and cyclic b_ε loading conditions, whereas no such unique relationship exists for other initial conventional fabrics (a_{pin}, a_{cin}, C_{in}, RI_{in}, and e_{in}). $MNPD_{in}$ thus emerges as an effective indicator for predicting final γ_{0s}. The correlation between $MNPD_{in}$ and γ_{0s} is slightly superior under cyclic b_ε loading compared to constant b_ε loading.

6 ACKNOWLEDGMENTS

The authors would like to thank the National Natural Science Foundation of China (No. 52425904 and 52378349) for funding the work presented in this paper. The work also received supported from the Tsinghua University Initiative Scientific Research Program.

7 REFERENCES

Da Cruz, F., Emam, S., Prochnow, M., Roux, J.-N., and Chevoir, F., 2005. Rheophysics of dense granular materials: Discrete simulation of plane shear flows. *Physical Review E*, *72*(2), 021309.

De Alba, P. A., Chan, C. K., and Seed, H. B., 1976. Sand Liquefaction in Large-Scale Simple Shear Tests. *Journal of the Geotechnical Engineering Division*, *102*(9), 909–927.

Hu, Q., Zhang, J.-M., and Wang, R., 2020. Quantification of dilatancy during undrained cyclic loading and liquefaction. *Computers and Geotechnics*, *128*, 103853.

Huang, X., Kwok, C., Hanley, K. J., and Zhang, Z., 2018. DEM analysis of the onset of flow deformation of sands: Linking monotonic and cyclic undrained behaviours. *Acta Geotechnica*, *13*(5), 1061–1074.

Kloss, C., Goniva, C., Hager, A., Amberger, S., and Pirker, S., 2012. Models, algorithms and validation for opensource DEM and CFD–DEM. *Progress in Computational Fluid Dynamics, an International Journal*, *12*(2–3), 140–152.

Satake, M., 1982. Fabric tensor in granular materials. In: Vermeer,P.A., Luger,H.J.(Eds.), Deformation and failure of granular materials. Balkema, Rotterdam, pp.63-68.

Wang, G., and Wei, J., 2016. Microstructure evolution of granular soils in cyclic mobility and post-liquefaction process. *Granular Matter*, *18*(3), 51.

Wang, R., Fu, P., Zhang, J.-M., and Dafalias, Y. F., 2016. DEM study of fabric features governing undrained post-liquefaction shear deformation of sand. *Acta Geotechnica*, *11*(6), 1321–1337.

Yang, Q., Zhang, J.-M., and Wang, R., 2025. Fabric quantities governing liquefaction resistance and post-liquefaction shear deformation of granular material. *Computers and Geotechnics*, *185*, 107344.

Zhang, J.-M., Shamoto, Y., and Tokimatsu, K., 1997. Moving critical and phase-transformation stress state lines of saturated sand during undrained cyclic shear. *Soils Found*, *2*.

Zhang, J.-M., and Wang, G., 2012. Large post-liquefaction deformation of sand, part I: Physical mechanism, constitutive description and numerical algorithm. *Acta Geotechnica*, *7*(2), 69–113.

Zhang, J.-M., and Wang, R., 2024. Large post-liquefaction deformation of sand: Mechanisms and modeling considering water absorption in shearing and seismic wave conditions. *Underground Space*, *18*, 3–64.